PNAS RESEARCH ARTICLE | ENGINEERING

Symmetry engineering in 2D bioelectronics facilitating augmented biosensing interfaces

Yizhang Wu[a,1], Yihan Liu[a,1], Yuan Li[b,c,1], Ziquan Wei[d], Sicheng Xing[a], Yunlang Wang[e], Dashuai Zhu[f], Ziheng Guo[a], Anran Zhang[a], Gongkai Yuan[a], Zhibo Zhang[g], Ke Huang[h], Yong Wang[e,i,2], Guorong Wu[d,j,k,l,2], Ke Cheng[f], and Wubin Bai[a,2]

Affiliations are included on p. 10.

Edited by John Rogers, Northwestern University–Evanston, Evanston, IL; received June 25, 2024; accepted October 7, 2024

Symmetry lies at the heart of two-dimensional (2D) bioelectronics, determining material properties at the fundamental level. Breaking the symmetry allows emergent functionalities and effects. However, symmetry modulation in 2D bioelectronics and the resultant applications have been largely overlooked. Here, we devise an oxidized architectural MXene, referred to as oxidized MXene (OXene), that couples orbit symmetric breaking with inverse symmetric breaking to entitle the optimized interfacial impedance and Schottky-induced piezoelectric effects. The resulting OXene validates applications ranging from microelectrode arrays, gait analysis, active transistor matrix, and wireless signaling transmission, which enables high-fidelity signal transmission and reconfigurable logic gates. Furthermore, OXene interfaces were investigated in both rodent and porcine myocardium, featuring high-quality and spatiotemporally resolved physiological recordings, while accurate differentiated predictions, enabled via various machine learning pipelines.

bioelectronics | symmetry engineering | machine learning | biosensing | logic matrix

Bioelectronics with two-dimensional (2D) materials enable paradigm-shifting diagnostic and therapeutic strategies, owing to a plethora of distinctive phenomena, such as rectification, the photovoltaic effect, and the quantum Hall effect (1–3). Of particular interest are these subjects that offer customized modes of operation enabled by these versatile components as electrical and optical interfaces across a range of spatiotemporal scales. Recent progress in such 2D bioelectronics establishes the basis for the seamless integration of microsystems technologies with living organisms, to provide persistent, multimodal function with applications in modulating cardiac cycles, deep-brain stimulation, regenerating sensorimotor functions, and many others (4–7). Thus, interfacing 2D bioelectronics with biological tissues represents a promising trend in probing and actuating biological systems. The broad central focus in 2D bioelectronics that requires reliable interaction between biological tissues and electronics is in the development of augmented biosensing interfaces, underlying a broad collection of application scenarios, featuring high-quality physiological recording with chronic stability and biocompatibility (8).

In this regard, symmetry engineering in 2D bioelectronic materials holds great promise to provide intrinsic augmentation in targeted functionalities. Conceptually differing from functionalized device integration, symmetric breaking offers a distinctive approach to improving signaling transmission or energy transduction beyond the conventional limitation imposed by inherent material properties. For example, the piezoelectric effect, featuring noncentrosymmetric materials, converts mechanical energy into electricity, furthering untethered, self-powered electronics (9, 10). Nevertheless, material symmetry is generally determined by its pristine crystallographic structure, and loss of symmetry usually occurs via phase transitions (11); Or the symmetry can be tuned by external stimuli, such as the flexoelectric effect induced by strain gradients (12), while is hampered by its rather small effective coefficients and a complicated setup for inducing large strain gradients (13). Thus, an alternative that is robust and spontaneous would be highly desirable for developing 2D bioelectronic interfaces based on symmetry breaking, while connecting these fundamental insights to real-world applications, especially in clinical practice.

We devise an oxidized-MXene (OXene) architectural composite that emphasizes decoupling the broken symmetry configuration into orbit symmetric breaking and inverse symmetric breaking, which cooperatively augments electron transport and response (Fig. 1*A*). Such augmentation implements the exploiting and coupling of additional out-of-plane electron conduction and built-in polar structures. The subsequently improved electronic-tissue impedance and Schottky-induced piezoelectric effect both enable the augmented biosensing interfaces via various device configurations. This approach allows

Significance

Symmetry lies at the heart of the laws of nature that form the basis of modern physics and determine material properties at the fundamental level. By regulating symmetry in mildly oxidized MXene (OXene) architectural composites, we achieve improved out-of-plane conductive pathways and Schottky-induced piezoelectric effects. The broad applicability of this augmented biosensing interface spans various wearable and implantable applications, including microelectrode arrays, gait analysis, active transistor matrices, and wireless signaling transmission. Our findings highlight significant advancements in signal fidelity and reconfigurable logic gates. Additionally, OXene's high-quality, spatiotemporally resolved physiological recordings in rodent and porcine myocardium, coupled with accurate predictions through machine learning, underscore symmetry engineering in two-dimensional (2D) bioelectronics will facilitate a paradigm shift in diagnostic, monitoring, and therapeutic strategies.

This article is a PNAS Direct Submission.

[1] Y. Wu, Y. Liu, and Y. Li contributed equally to this work.

[2] To whom correspondence may be addressed. Email: yongwang@xidian.edu.cn, guorong_wu@med.unc.edu, or wbai@unc.edu.

This article contains supporting information online at https://www.pnas.org/lookup/suppl/doi:10.1073/pnas.2412684121/-/DCSupplemental.

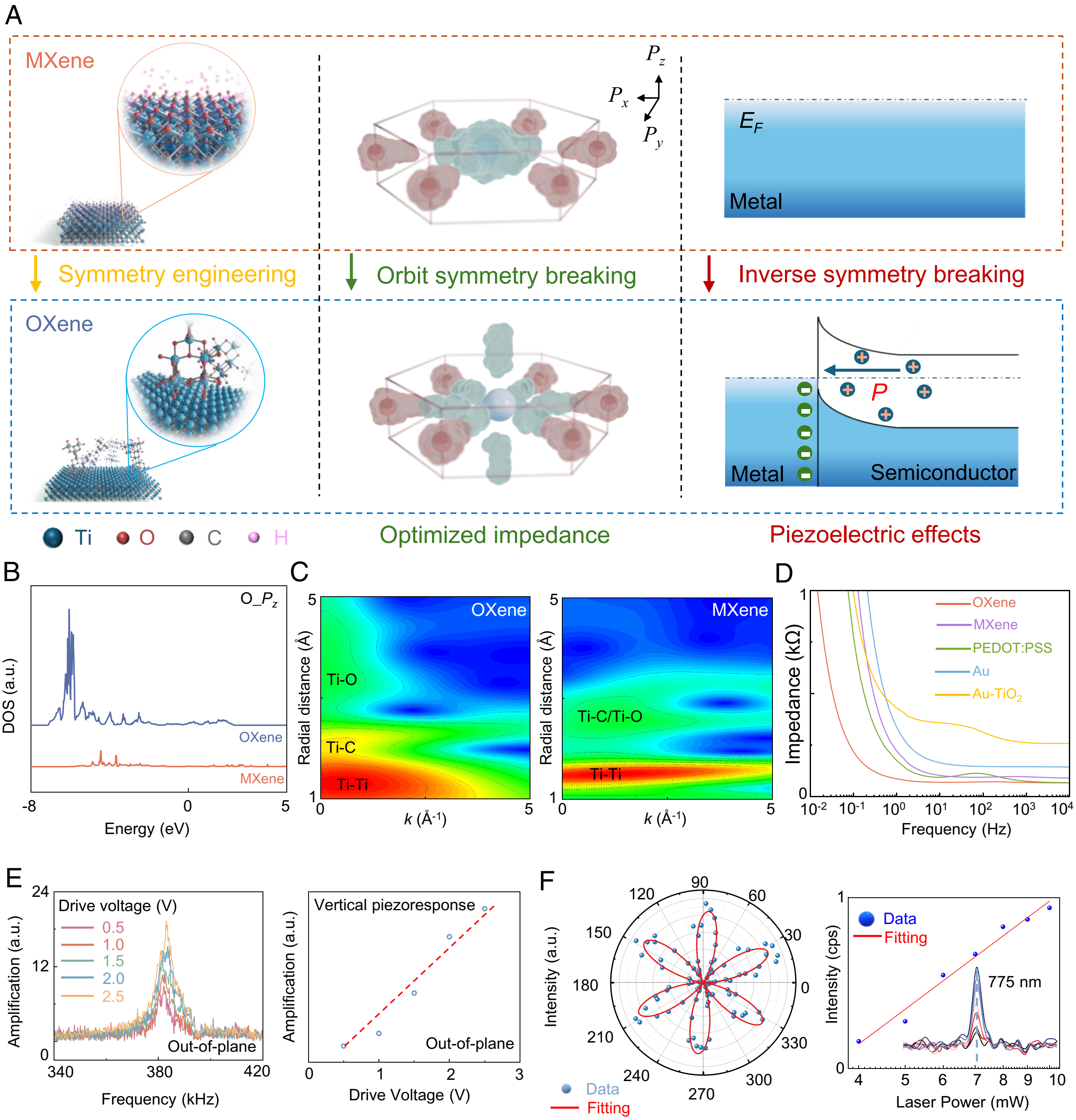

Fig. 1. Dual symmetry engineering in 2D bioelectronics implements the augmented sensing interface. (*A*) Schematic illustration of the principle of dual symmetric engineering in OXene, which originates from orbital and inverse symmetric breaking, enabling the applications of microelectrode array, gait analysis, reconfiguration transistors, and wireless transmission. (*B*) PDOS of O atoms projected on the P_z orbital in OXene and MXene ($Ti_3C_2O_x$). PDOS, projected density of states. (*C*) Morlet wavelet transforms of Ti *K*-edge k^2-weighted EXAFS spectra for OXene (*Left*) in comparison to that of lyophilized monolayered MXene (*Right*). EXAFS, extended X-ray absorption fine structure spectroscopy. (*D*) Electrochemical impedance spectra (EIS) measured in 5 mM $K_4[Fe(CN)_6]/K_3[Fe(CN)_6]$ (1:1) solution for the OXene electrode in comparison to that of MXene, Au, Au-TiO_2, and poly(3,4-ethylenedioxythiophene) polystyrene sulfonate (PEDOT:PSS) electrodes. (*E*) Vertical resonance peaks (left) of OXene at approximately 385 kHz with gradient voltages, showing linearity of the vertical resonance peak (*Right*) intensity concerning the drive voltage (ranged 0.5 V to 2.5 V, 0.5 V intervals). (*F*) Polar plot (*Left*) and excitation power plot (*Right*, log–log scale) of the SH intensity from monolayer OXene as a function of the crystal's azimuthal angle θ. (*Inset*) SHG spectra of the various excitation powers. The SH component is measured perpendicular to the excitation polarization. Second harmonic generation (SHG).

for extensive versatility for varying 2D bioelectronic applications, including bioelectrode array, gait analysis, wireless implants, and reconfigurable computational substrate in transistors, with capabilities of high-fidelity operation and scalable spatiotemporal resolution. Incorporated with machine learning (ML) pipelines, data obtained by OXene-infused interfaces can be used to classify physiological signals at high accuracy and provide reliable predictions on potential adverse events.

Synthesis of OXene leverages a facile strategy (*SI Appendix*, Fig. S1*A*), with three primary steps: i) constructing intrinsically conductive traces by solution processable MXene, ii) implementing on-demand transformation by laser cutting, iii) deriving anatase TiO_2 on the surface by oxygen plasma treatment, collectively as the key innovation. Completely isolated symmetry-breaking induction facilitates OXene with capabilities to realize local region customizations upon varying functional bioelectronics. Besides, electrochemical impedance of OXene is tunable by varied oxygen plasma treatment (*SI Appendix*, Fig. S1*B*).

The controlled oxidization process of MXene may play a proximate role in the strain gradient in terms of symmetry engineering, lowering or even breaking the symmetry. Morphologies of OXene reveal spindle-shaped anatase TiO_2 (14) immobilized at flake edges (*SI Appendix*, Fig. S2 *A–D*). OXene preserves the basic infrastructure of MXene, while reorganizing the surface dangling bonds and regulating the out-of-plane vibration (*SI Appendix*, Fig. S3). The derived oxides, localizing charge in the form of polarons on metallic surfaces, can act as deep-state point defects, which renders a charge transfer pathway differing from pristine planar electron transport (*SI Appendix*, Fig. S2*E*). Besides, evidence that anatase TiO_2 sustains large electron polaron, which promotes the frontier orbitals (conduction-band minima, CBM) made up of weakly interacting orbitals and a high density of states around the band edges, favoring symmetry reduction (15). Theoretical calculations (Fig. 1*B* and *SI Appendix*, Fig. S4) predict that *p-d* hybridization alters orbital symmetry in OXene, leading to the misalignment of metallic *d*-orbitals with t_{2g} symmetry and O 2*p* orbitals (16). Besides, a dipole transition in OXene features Ti *1s* orbital to the *p*-component (*SI Appendix*, Fig. S4*D*), specifically to projected P_z orbital of oxygen, which is distinguished from other titanium species (e.g., compounds, monomers, and oxides) (Fig. 1*C* and *SI Appendix*, Fig. S5). Symmetry breaking in P_z orbitals realigns out-of-plane vibrations in *R*-space (*SI Appendix*, Fig. S5*D*), with the capability of actively participating in electron transfer (17).

The out-of-plane electron transfer leads to a decreased interfacial impedance (Fig. 1*D* and *SI Appendix*, Fig. S6), compared with other common bioelectrical materials (e.g., Au, PEDOT:PSS, MXene, and Au-TiO_2). The derived TiO_2 facilitates a heterogeneous semiconductor–metal interface while creating a depletion or space charge region. Double-layer capacitance (C_{dl}, *SI Appendix*, Fig. S6*E*) consequently forms in the presence of electrolytes, accompanied by anisotropic out-of-plane/in-plane electron conduction, which contributes predominantly to reducing impedance (18). The charge transfer resistance (R_{ct}, *SI Appendix*, Fig. S6*G*) in OXene, providing high charge-carrier mobility, also optimizes its interfacial impedance.

The derived oxides are coupled with metallic substrates, considering the varying terminal groups (–F, –OH, and =O), that enable to form metal–semiconductor contacts termed Schottky junctions (*SI Appendix*, Fig. S7). Schottky junctions feature a rather strong built-in field, modulating the partially filled valence Ti *d*-orbitals (*SI Appendix*, Fig. S8*S*), which allows the rearrangement of the energy levels for aligning the Fermi level (*SI Appendix*, Fig. S8*B*). Schottky barrier renders charge accumulation in metallic substrates while a depletion region within the anatase TiO_2 (*SI Appendix*, Fig. S8*C*) (19). The carrier tunneling behavior (*SI Appendix*, Fig. S8*D*) also enhances the built-in electrical field and induces interface polarization (20). Massive charge transfer and redistribution lead to discontinuities in the interfacial potential and the presence of interface dipoles (21).

Schottky junction induces the piezoelectric effect in OXene, showing deformation aligned linearly with potential, whereas MXene barely exhibits a piezoelectric excitation (*SI Appendix*, Fig. S9). After eliminating morphological effects employing dual frequency resonance tracking, we achieve uniform and stable out-of-plane and in-plane piezoelectric responses (*SI Appendix*, Fig. S10). Phase signals (*SI Appendix*, Fig. S10*B*) illustrate a consistent polarization direction with the electrical field, demonstrating the presence of piezoelectric dipoles in OXene (22). The piezoelectric response in OXene is aligned with the simple harmonic oscillator model, conforming to out-of-plane (first harmonic) and in-plane (second harmonic) resonance peaks (Fig. 1*E*). OXene shows a higher second harmonic response than the first harmonic response (*SI Appendix*, Fig. S11), underlying piezoelectricity primarily arises from polar dipoles rather than spontaneous polarization or electrostatic interference (23). Polarization-resolved SHG displays a trifold rotational symmetry dependent on the azimuthal angle of monolayer OXene (Fig. 1*F*). The SH response stems from the broken inversion symmetry. Asymmetric engineering results in local polarization via the polar nature of the built-in field, emerging piezoelectric effects (24). Accordingly, dual symmetry breaking in OXene promises to facilitate a variety of practical bioelectronics with the fundamental principles.

OXene-Infused Bioelectrode Interfaces for Pathological Prediction

Improving interfacial impedance at the electronic–tissue interface potentially renders high-fidelity signaling transport and built-in signal amplification for implantable sensors. To demonstrate enhanced interfacial impedance enabled by OXene, we interfaced a 3 × 3 bioelectrodes array with the rat epicardium under sinus and myocardial infarction (MI) (Fig. 2*A* and *SI Appendix*, Fig. S12*A*). The multichannel electrode captures electrocardiography (ECG) covering the Left ventricle (Fig. 2*B*). Built on a flexible styrene-ethylene-butadiene-styrene (SEBS) substrate (~20 μm), this array conformally laminates on the epicardium against rhythmic cardiac systole and diastole (Fig. 2*C*, *SI Appendix*, Fig. S12*B*, and Movie S1).

To comprehensively characterize the signal qualities, we compared unfiltered raw data using unified variable (heart status, and device orientation) OXene, MXene, and polyvinylidene fluoride or PVDF bioelectrodes collected from various rodent models with Sinus (refer to the normal healthy sinus rhythm) or MI conditions (*SI Appendix*, Fig. S12*C*). Myocardial mechanical motions can contaminate electrophysiological signals with unwanted noise. Decreased impedance in OXene at the electronic–tissue interface ensures superior signal fidelity and higher signal-to-noise ratio (SNR) compared with MXene, enabling more precise cardiac monitoring. Specifically, OXene-infused bioelectrodes allow for clearly delineating P wave and QRS complex in the acute infarction model (Fig. 2*D*), which is characterized by slow atrial depolarization and conduction system dysfunction (25). This clarity stems from decreased interfacial impedance and is crucial for assessing patient cardiac status in clinical settings. Conversely, signals collected from MXene electrodes exhibit baseline fluctuations and inferior signal noise, which did not clearly show the process of atrial depolarization (P wave) and ventricular repolarization (T wave).

The high recording performance offered by the OXene-infused interfaces enables high-fidelity ML evaluations to predict pathological risks of cardiac tissues at an early stage. The observation on the OXene signal distribution (Fig. 2*F*) shows a separate cluster of cardiac diseases (e.g. MI), where each point that is a nine-channel vector is closer to each other under the same cardiac status in a 2D space, using the TSNE dimensionality reduction algorithm, which preserves the relationship between the original data points. To quantitatively measure the benefit of OXene on Sinus/MI classification, we comprehensively test a DNN (Fig. 2*E*) that corporates with the 8-way-1-shot supervised learning, i.e., each class has one data point for training the DNN, in all possible cases. DNNs excel at processing high-dimensional, nonlinear data, which is particularly important when dealing with multichannel signals that contain subtle, complex patterns not easily captured by traditional

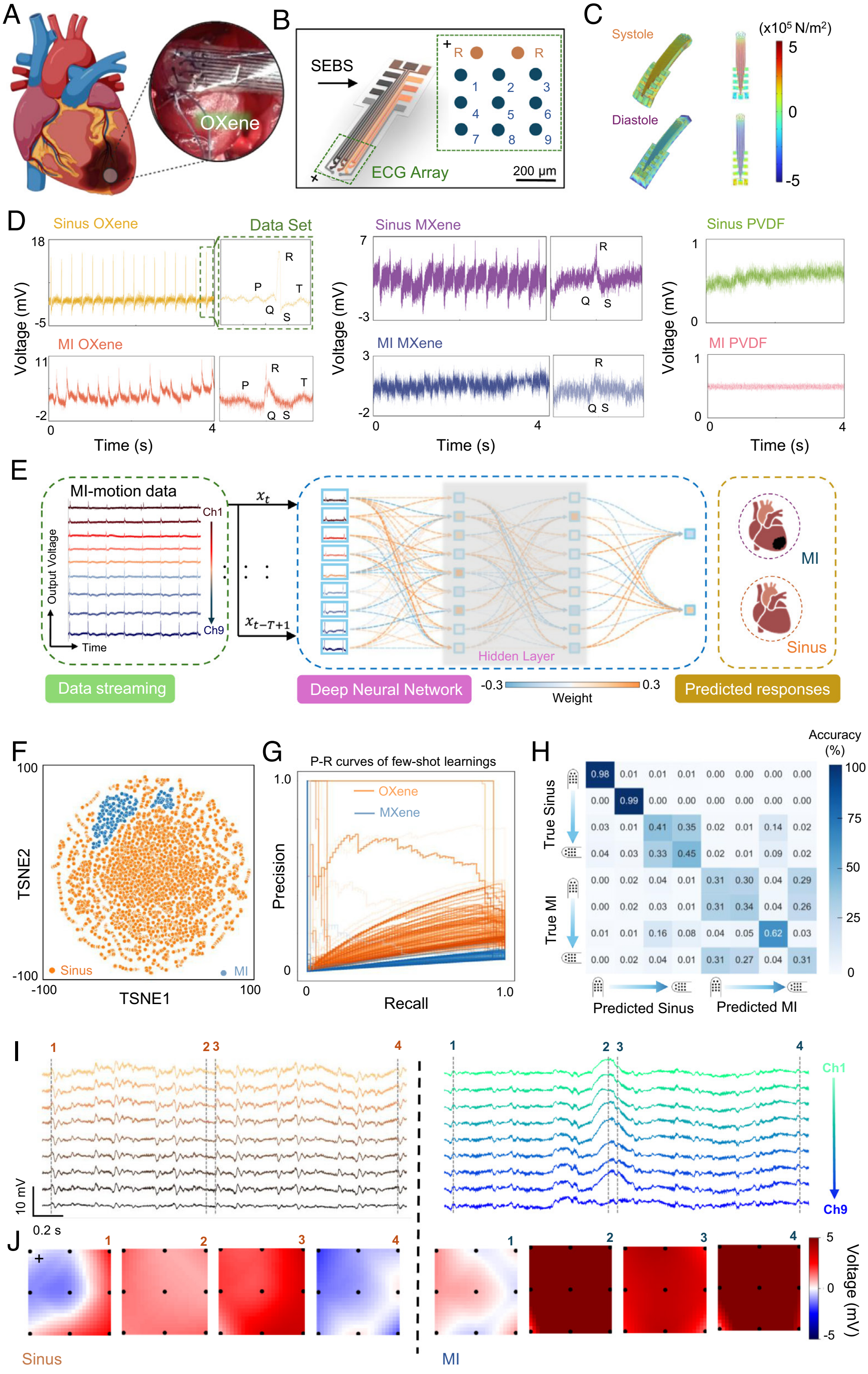

Fig. 2. Orbit symmetric breaking in OXene enhances the performance of the bioelectric interface and enables physiological prediction powered by ML. (*A*) An optical image of the OXene-based multichannel electrodes mounted to the rat epicardium. Coronary artery ligation was performed in the left ventricle to simulate acute MI. (*B*) Schematic illustration of a 3 × 3 OXene electrode array, illustrating the size and serial number of each unit. Elastomeric SEBS substrate enables conformal and stretchable attachment on the epicardium. (*C*) Simulation results for the distribution of systole and diastole stresses at the interface between the electrode array and underlying cardiac tissue during biaxial stretching. (*D*) Evaluation of unfiltered raw data obtained from rat myocardium w/wo MI upon OXene, MXene, and polyvinylidene difluoride (PVDF) electrodes featuring the 90° (*Left*) device orientation on the epicardium and the selected data recorded from the fourth channel of the nine-channel array. P wave represents the atria depolarization; QRS complex stands for integrated Q wave, R wave, and S wave complex, representing ventricular depolarization; ST segment represents the interval between ventricular depolarization and repolarization. (*E*) Schematic illustration of the ML architecture for data preprocessing, deep neural network (DNN), and predicated responses, anticipating an MI or a sinus electrophysiological status. Sinus electrophysiological status refers to the normal healthy sinus rhythm. (*F*) *t*-distributed stochastic neighbor embedding (TSNE) plot from the OXene dataset, visually showing feature separation (sinus and MI) in a 2D space. (*G*) Precision–recall curve of few-short learnings classified from OXene and MXene interface. (*H*) Confusion matrix displaying the spatial distribution accuracy for predicting either Sinus or MI in the OXene dataset. (*I*) Segments of the recorded ECG signal from the OXene electrode array on a living rat heart with sinus rhythm (*Left*) and MI (*Right*). The data are displayed following the spatial arrangement of the electrode array (*B*). (*J*) Instantaneous electrophysiology mapping using OXene electrodes corresponds to sinus rhythm (*Left*) and MI molding (*Right*). The mapping frames selected here correspond to the respective four synchronous points highlighted by the vertical dashed lines in *I*.

methods. Accuracy comparison of precision–recall curves (Fig. 2*G*) illustrates that OXene mostly outperforms MXene, which tends to be solely high on recall or precision. Additionally, six classes of OXene are more accurate than MXene on the confusion matrix (Fig. 2*H* vs. *SI Appendix*, Fig. S13*A*) where the deep learning task involves different locations of the sensor settled, four for Sinus/MI as mentioned above, leading to an eight-class classification. In case they are separately trained, 3 out of 4 locations show that OXene enables better performance on the confusion matrix (*SI Appendix*, Fig. S13 *B* and *C*). Such superiority of OXene to recognize cardiac disease is supported by the higher accuracy (0.9 to 1.0) on train and evaluation curves (*SI Appendix*, Fig. S13 *D*–*G*). In the case of MXene, the features extracted by the DNN are less informative, leading to lower classification accuracy.

OXene array is capable of spatial and temporal mapping over large areas of the heart. Representative sinus and MI segments are intercepted, while selecting four R-wave (represents the maximum amplitude in QRS complex) timestamps (Fig. 2*I*). Instantaneous ECG mapping can be interpolated across the matrix and normalized, illustrating the propagated spatial disparities in electrophysiological activity between the sinus and MI models over time. It should be noted that the spatial resolution can be further extended with denser sensing nodes.

The OXene array not only captures localized ECG fragments but also records long-term cardiac activity, featuring consistently high SNR and spatiotemporal resolution (*SI Appendix*, Fig. S14). Besides, OXene-based microelectrode array facilitates higher spatial resolution due to its decreased interfacial impedance and scalable fabrication process (*SI Appendix*, Fig. S14 *E–I*). The expanded and dynamic ECG mapping (Movie S2) offers further insights into arrhythmia pathogenesis and can be synchronized with structural computed tomography images of the heart for precise arrhythmia focus localization. In this view, solution-processable OXene traces also approach them as excellent coatings on the electrode surface of existing commercially implantable electronics including cardiac pacemakers, neurostimulators, deep brain stimulators, and others, for augmented biosensing interfaces.

Schottky Interface from OXene-Filled Composite for Gait Analysis

Piezoelectrically mediated OXene allows extra polarized charges with external stress via electrostriction effect, promising to achieve impressive signal sensitivity in pressure sensing electronics.

To visualize and quantitatively characterize the piezoelectric effect, we designed an OXene-filled ionogel architecture anchored onto the interdigital electrodes for gait analysis (Fig. 3*A*). The choice of the specific ionogel as pressure modules were motivated by its ionic conductivity, ultra-toughness, and stretchability (26). These ionogels consist of hydrogen-bonded domains connected by highly solvated and soft domains to form an extremely tough ionogel (Fig. 3*B*), enabling stable and uniform dispersing of pressure from curved surfaces (*SI Appendix*, Fig. S15*A*). Whereas the high fracture strength (21.6 MPa) and Young's modulus (35.9 MPa) of ionogels consequentially contribute to strain insensitivity and signal vulnerability (*SI Appendix*, Fig. S15 *B* and *C*). Besides, ionogels featuring various thickness maintain a linear and monotonic stress-voltage response (*SI Appendix*, Fig. S15*D*), ensuring the sensing effectiveness.

OXene flakes form in-plane conductive percolation networks that are strongly crosslinked via hydrogen bonding using electrostatic self-assembly. The anatase TiO_2 isolated from in-plane networks facilitates anisotropic out-of-plane electrical conduction (Fig. 3*C*). Consequently, the built-in field-induced piezoelectric effect allows for charge redistribution at the Schottky interface under tensile or compressive forces (Fig. 3*D*), resulting in interlayer displacement of charge carriers that correspondingly augment the sensitivity of the stress response. The piezoelectric effect of OXene (derived from Schottky-induced inversion symmetry breaking) enables a unique advantage over piezoelectric PVDF films in improving the signal sensitivity of pressure-mediated sensing electronics (*SI Appendix*, Fig. S15 *E–G*).

Mechanistically, we performed a dynamic theoretical calculation to intuitively simulate the band structure subjected to varying strains (*SI Appendix*, Figs. S16–S18). The deformation facilitates a transition from P-type Schottky contact to N-type Schottky contact or N-type quasi-ohmic contact within OXene, redistributing the charge between the metal and semiconductors to reach a new equilibrium state (27). Subsequently, the effective barrier of the Schottky junction, featuring insulating properties, prevents the polarized electrons from flowing across the interface directly, thus outputting electricity through the external circuit (28). Meanwhile, the built-in field under mechanical strain achieves enhanced electric polarization in the depletion region (*SI Appendix*, Fig. S19), as a driver for the efficient separation of electron–hole pairs (29). Among these, the density of states of Ti atoms near the Fermi level dominates the piezoelectric polarization process. It is worth noting that the basic Schottky model is used here for simplicity, without considering the electric-field-dependent permittivity and anomalous capacitance-voltage characteristics.

Compared with MXene-enriched ionogels, OXene-enriched ionogels indicate a markedly enhanced pressure response (Fig. 3*E*). We then deployed a real-time control system on the subject, including an OXene-infused multimatrix sensor, clock signal generator, signal preprocessing circuit, and MCU with wireless transmitter module (Fig. 3*F* and *SI Appendix*, Fig. S20). Notably, the adaptation of an analog-to-digital converter allows sampling of the impedance magnitude of the composite, rather than the resistance, avoiding signal drift and inaccurate measurement caused by the viscoelastic creep of the soft materials (*SI Appendix*, Fig. S21) (30). This sensory system allows for the continuous and synchronous capturing of the pressure distribution on the sensing pixels featuring drift-free signals under prolonged high stresses (Fig. 3*G* and Movie S3).

OXene-infused ionogel, featuring highly sensitive and stable sensing capabilities, offers superior recognition accuracy and prediction with recurrent neural network pipelines. The algorithm (Fig. 3*H*) starts with the data acquisition from eight different sensors, followed by real-time preprocessing to filter out the unwanted noise and remove the baseline shift. A feature extraction approach then recognizes the gait patterns from the preprocessed signals (*SI Appendix*, Fig. S22) and passes them to the GRU model, which eventually predicts gait attribution. A PCA shows the variation of all 924 signal samples collected from on-body tests (Fig. 3 *I* and *J*). The distribution of the three most significant PCs demonstrates the differentiable distribution of the samples due to the compelling clustering (Fig. 3*I*). The weight of the select feature was elaborated on each PC, distinctly demonstrating the similarity within the data from each foot and the disparity between the two feet (Fig. 3*J*). Piezoelectrically actuated OXene ionogels, featuring the high-sensitive data stream, enable the augmented classification over MXene-based counterparts (*SI Appendix*, Fig. S23). The training curve shows an evident convergence based on the tendency of the loss toward 0 and the accuracy toward 1 at around the 100th epoch (Fig. 3*K*). The corresponding confusion matrix shows that 11 of the 13 labels have a prediction accuracy exceeding 85% (Fig. 3*L*). The remaining three labels, despite being lower than 85%, still show the maximum value at the correct prediction among all possible ones. The predicted score of all 924 samples is highlighted in the sequence of the true label from 1 through 13 (Fig. 3*M*), confirming that the ML-assisted pressure array based on OXene-filled ionogels can offer a precise gait prognosis.

Piezoelectric OXene is capable of highly sensitive pressure detection, not only augmenting the soft elastomer, but also promising to interact with other artificial haptic technologies involving pressure interfaces, such as robotic haptics, automatic pilot and drive, and virtual reality, achieving reliable control and manipulation of an artificial robot.

OXene-Mediated Reconfigurable Logic in Flexible field effect transistor

Reconfigurable logic circuits, enabled by field effect transistor (FET) technology, offer denser, faster, and more energy-efficient alternatives to conventional transistor circuits (31). Facile oxygen

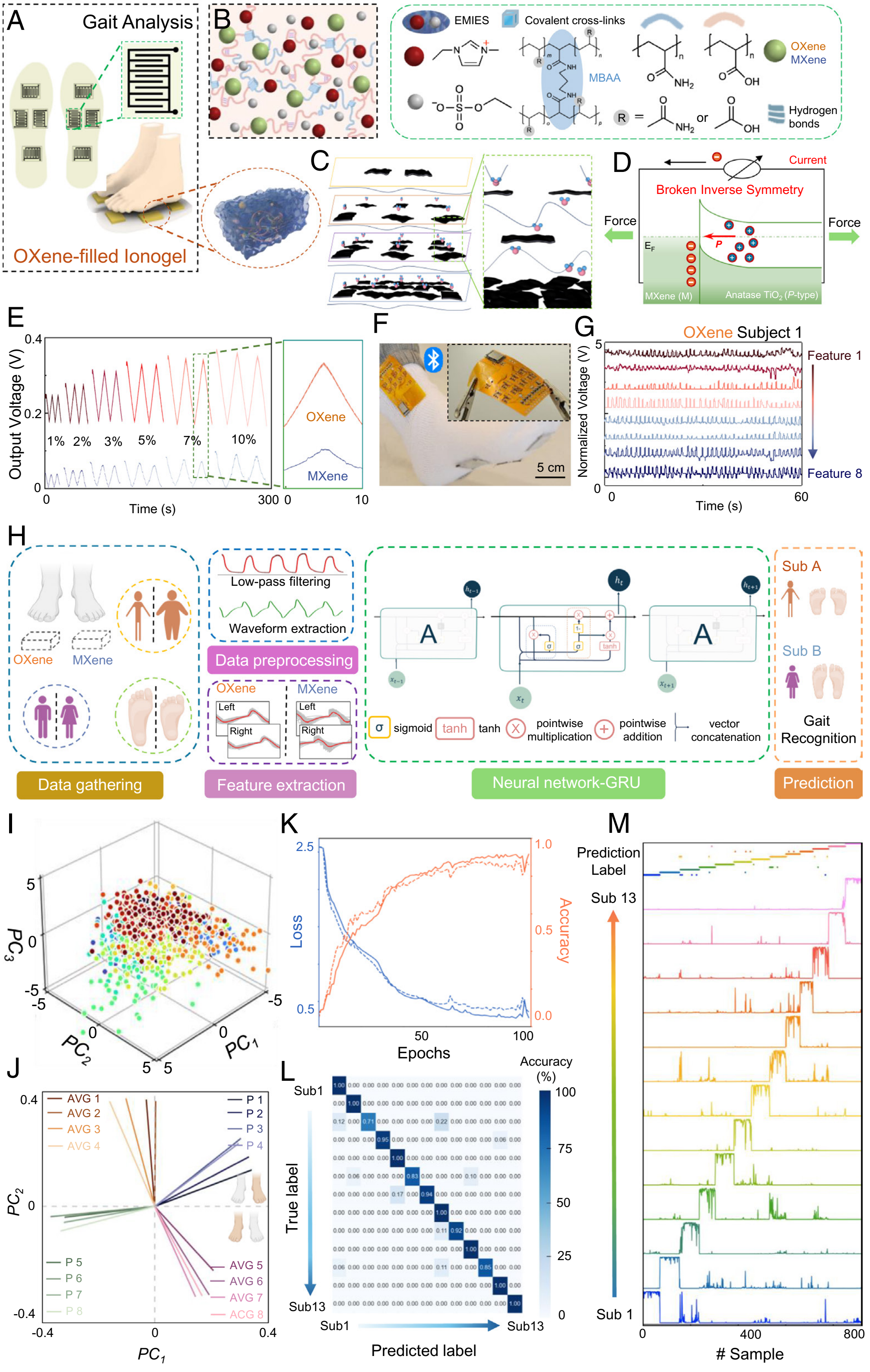

Sub1	1.00	0.00	0.00	0.00	0.00	0.00	0.00	0.00	0.00	0.00	0.00	0.00	0.00
	0.00	1.00	0.00	0.00	0.00	0.00	0.00	0.00	0.00	0.00	0.00	0.00	0.00
	0.12	0.00	0.71	0.00	0.00	0.00	0.00	0.22	0.00	0.00	0.00	0.00	0.00
	0.00	0.00	0.00	0.95	0.00	0.00	0.00	0.00	0.00	0.00	0.00	0.06	0.00
	0.00	0.00	0.00	0.00	1.00	0.00	0.00	0.00	0.00	0.00	0.00	0.00	0.00
	0.00	0.06	0.00	0.00	0.00	0.83	0.00	0.00	0.00	0.10	0.00	0.00	0.00
	0.00	0.00	0.00	0.00	0.17	0.00	0.94	0.00	0.00	0.00	0.00	0.00	0.00
	0.00	0.00	0.00	0.00	0.00	0.00	0.00	1.00	0.00	0.00	0.00	0.00	0.00
	0.00	0.00	0.00	0.00	0.00	0.00	0.00	0.11	0.92	0.00	0.00	0.00	0.00
	0.00	0.00	0.00	0.00	0.00	0.00	0.00	0.00	0.00	1.00	0.00	0.00	0.00
	0.06	0.00	0.00	0.00	0.00	0.00	0.00	0.11	0.00	0.00	0.85	0.00	0.00
	0.00	0.00	0.00	0.00	0.00	0.00	0.00	0.00	0.00	0.00	0.00	1.00	0.00
Sub13	0.00	0.00	0.00	0.00	0.00	0.00	0.00	0.00	0.00	0.00	0.00	0.00	1.00

Fig. 3. Inverse symmetric breaking in OXene serving as ionogel fillers augments pressure sensitivity. (*A*) Schematic diagram of the sensor layout. The signaling input was achieved by OXene-filled pressure sensing ionogels mounted on interdigital electrodes. Targeted regions for pressure sensing feature the anterior transverse arch, medial longitudinal arch, lateral longitudinal arch, and heel, discriminating individual behavior. (*B*) Schematic illustration showing a molecular network of the OXene/MXene-filled ionogels. 1-ethyl-3-methylimidazolium ethyl sulfate (EMIES) coupling with poly(acrylic acid) (PAA) polymers and Poly (acrylamide) (PAAm) polymers form a stiff but brittle polymer network. The electronegative OXene/MXene fillers are uniformly distributed in the matrix of the ionogel via hydrogen bonding with an electrostatic self-assembly mechanism. The ingredients of the ionogel and the corresponding molecular structure formula are listed on the *Right*. (*C*) Schematic illustration of OXene-filled ionogels. (*Left*) The electronegative fillers are anchored in the planar domains due to the negatively charged surface and the positively charged ion chains by hydrogen bonds. (*Right*) Interlaminar anatase TiO_2 bridging the electron transfer channel among the confined in-plane nanoflakes. (*D*) Schematic illustration of a Schottky junction constructed from metallic MXene and P-type anatase TiO_2 showing a potential modulation in the depletion region with a built-in field. The piezoelectric effect is induced by the Schottky interface's inverse symmetry breaking, resulting in charge redistribution when the Schottky junction is subjected to a tensile/compressive force. (*E*) Real-time measurements of relative voltage outputs of OXene/MXene-filled ionogel (*Left*) and localized segments (*Right*) with cyclic strains, indicating a superior strain sensitivity from OXene fillers. (*F*) Optical image of an OXene-filled gait sensor settled on a human subject, consisting of a four-ionogels group (signaling interface) and a flexible microcontroller unit (MCU, main functionalities: signal amplification, filtering, and Bluetooth signaling transmission). (Scale bar, 5 cm.) (*Inset*) Detailed circuit board of flexible MCU. (*G*) Spectrum of wireless gait sensing data featuring multichannel time synchronicity gathered from one subject. All signals were calibrated and normalized to against patch variations and any motion artifacts above a moderate level. (*H*) Data processing protocol. From *Left* to *Right*: i) Data gathered from subjects with different foot sizes, using OXene- and MXene-filled gait sensors, respectively. ii) Data preprocessing and feature extraction from the collected data from gait sensors. The step peaks from both *Left* and *Right* feet are extracted from the denoised signal. iii) Neural-network-based gait type classification algorithm, highlighting the layer of gated recurrent units (GRU). iv) Prediction generation based on the classification algorithm that yields the predicted gait type among all the input types. (*I*) Scatter plot showing the distribution of the three leading principal components (PCs) in the principal component analysis (PCA) of all the extracted features on 16 selected features. (*J*) Proportion of all 16 selected features in the first two PCs. (*K*) Training curve of the classification algorithm. Solid lines show the curves for training data, while the dashed lines show the curves for test data. Blue lines: Loss curves. Orange lines: Accuracy curves. (*L*) Confusion matrix for the model. *Y*-axis: true label. *X*-axis: predicted label. (*M*) Prediction score for all samples (*x*-axis). On the *y*-axis, it shows the scores of each sample on each prediction label (Subject 1 through 13, from bottom to top). The topmost plot shows the overall prediction after calculating the max value of the prediction scores.

treatment of OXene modifies its interaction with the upper semiconductor layer, enabling the creation of reconfigurable computational substrates that can change logical functions.

To investigate the emergent logic gates, we correspondingly fabricated the 5 × 5 active transistor matrix with side gate architecture, including i) polydimethylsiloxane (PDMS) as substrate and encapsulation layers; ii) large-area, uniform metallic OXene/MXene traces as the source-drain-gate (SDG) layer; iii) a blend of poly(3-hexylthiophene-2,5-diyl) nanofibrils and PDMS (P3HT-NFs/PDMS) as the semiconductor layer; iv) PVDF-HFP mixed with [EMIM][TFSI] as the dielectric layer (Fig. 4*A*). While we showcase a 5 × 5 array, it is noted that increasing the density of sensing nodes is feasible by reducing both the linewidth and the area of each sensing cell. Each pixel operates as a p-channel metal–oxide–semiconductor transistor, with gate electrodes of each column linked to a word line (V_{WL}) and source electrodes of each row connected to a bit line (V_{BL}). This transistor array endured various mechanical deformations, including stretching, poking, and crumpling, without sustaining physical damage (Fig. 4*B* and Movie S4), promising to establish conformable contact with tissue.

OXene and MXene characterize distinct transfer curves with differing on/off ratios, enabling the formation of reconfigurable computational substrates representing "0 and 1." The transfer-curve peak of OXene shows an on/off ratio exceeding 10^5, illustrating ideal charge-carrier mobility, a 10^4-fold improvement over MXene with the identical semiconductor and dielectric layers (Fig. 4*C*). Besides, the switching ratio of OXene transistors varies from 10^3 to 10^5 based on the duration of oxygen treatment, eventually reaching saturation (Fig. 4*D*).

OXene-mediated FET displays an impressive p-type output curve across varying gate voltages (V_{GS}) (Fig. 4*E*). The output curve indicates nonlinear behavior in the pre-V_{DS} region and saturation behavior in the post-V_{DS} region. Nonlinearity in the pre-V_{DS} region stems from Schottky contact, comprising: i) the OXene's internal and ii) OXene-semiconductor layers. Built-in field bending at the Schottky interface suppresses hole-electron recombination, enabling the output curve to achieve a record-high drain current (0.23 ± 0.02 mA) among reported P-type MXene-based FET [the best previous report was 0.094 mA to our knowledge (32)], while three orders of magnitude above unoxidized transistors. The derived TiO_2 acts as an N-type semiconductor, forming a P-N heterojunction with P-type P3HT, facilitating directional electron transfer analogous to P-doping in P3HT. Conversely, pristine MXene, with its electronegative surface, traps electropositive holes in P3HT, creating a depletion layer that hinders carrier movement in P3HT, akin to N-doping in p-type semiconductors (Fig. 4*F*).

To demonstrate reconfigurable logic gates, we devised NAND and NOR circuits based on OXene/MXene coexistence traces through selective oxidation *via* shadow masks, integrating with P-type P3HT. For NAND circuits, two drives (T_D) are aligned in parallel, whereas for NOR, they are arranged in series. These configurations randomly mix OXene and/or MXene elements to produce four distinct SDG designs, each then serially connected to an OXene-based load transistor (T_L). The reconfigurable logic gates introduce a new programmable dimension, yielding 16 functional outcomes. Specifically, in the NAND configuration, the logic state 1 occurs in seven of the combinations, while nine to the frequency of the logic state 0, thus maintaining a 7:9 output distribution ratio (Fig. 4*G*). This departs from the standard 1:3 ratio, improving signal integrity by reducing bias and timing skew. This equilibrium simplifies digital designs and lowers component needs, beneficial for fast and intricate computational systems (33). In the NOR configuration, a unique 1:15 "1 and 0" ratio enhances gate specificity and selectivity, promising more nuanced, condition-specific logic operations (Fig. 4*H*). Remarkably, this reconfigurability stems from dual symmetry breaking, altering the physical properties of the original SDG layer, rather than stacking functional layers. This flat architecture promises customizable logic functions within a compact, energy-efficient framework.

We further developed a fully flexible pressure sensing matrix to demonstrate the viability of the reconfigurable logic gates in bioelectronics (Fig. 4*I*). Our approach involves: i) constructing a 5 × 5 active pressure sensing matrix with either OXene or MXene mediated SDG layer, resulting in the distinct voltage transfer characteristics, ii) forming the epitaxial drain by using OXene-infused ionogels interconnected with conductive via-holes, and iii) aligning ionogels with OXene electrode arrays on flexible substrates, supplying the drain voltage. This flexible architecture allows for uniform force distribution, even under 10% biaxial deformation, facilitating the conformal interfaces deployed on soft tissues (*SI Appendix*, Fig. S24). We applied stresses both perpendicular and parallel to the channel length direction, mimicking the tactile sensation of skin (Fig. 4*J*). OXene-mediated FET arrays enable recognition of the geometric distribution of tactile sensations, over four orders of magnitude higher in sensitivity than that of MXene, thus allowing the former termed as the logic state 1, while the latter as 0 (Fig. 4*K*).

Wireless Monitoring and Spatiotemporal Mapping with OXene-Integrated Implants for ML-Enabled Clinical Prediction

Wireless bioelectronics facilitate full implantation into the body to eliminate the need for percutaneous hardware, thereby minimizing the risk of device-associated infections and dislodgement (34, 35). Development of untethered OXene-integrated implants, decisive for its practical clinical applications.

We present a flexible, biocompatibility, and leadless OXene cardiac patch that operates in a battery-free fashion and permits externalized control through resonant inductive coupling (Fig. 5*A*). In vivo validation using a porcine whole-heart model, closely mirroring human physiology, underscores its clinical applicability due to bearing a high resemblance of porcine cardiovascular system to that of humans (*SI Appendix*, Fig. S25*A*) (36). The fabrication approach consists of i) upper OXene bioelectrodes for pacing, ii) lower OXene ionogels for visualizing myocardial cycles (Fig. 5*B*), and iii) extended passive electromagnetic resonance sensing and magnetic resonance wireless power transfer coil embedded in porcine dermis for power and signal transmission (*SI Appendix*, Fig. S25 *B–D*).

This architecture integrates distributed wireless sensor and actuator networks to monitor and modulate cardiac physiological activity. The stimulator can generate an electrical field approaching 3 V/mm near the inner electrode with a 5 V DC input, alleviating slow ventricular depolarization and conduction-system dysfunction during acute myocardial ischemia (*SI Appendix*, Fig. S25*E*) (37). Fully flexible mechanical layouts ensure a seamless interface with the epicardium and concurrently deform with the beating heart (Fig. 5*C* and *SI Appendix*, Fig. S25*F*).

OXene-integrated wireless implants maintain stable function throughout the postoperative period. OXene-filled ionogel exhibits a monotonic correlation between pressure-induced capacitive change and resonant frequency (Fig. 5*D*), which can be quantified via a vector network analyzer (VNA). Clinically, a VNA probe aligns with an underchest soft inductor coil, facilitating wireless signal transmission a week post-MI surgery (Fig. 5*E*). It entitles

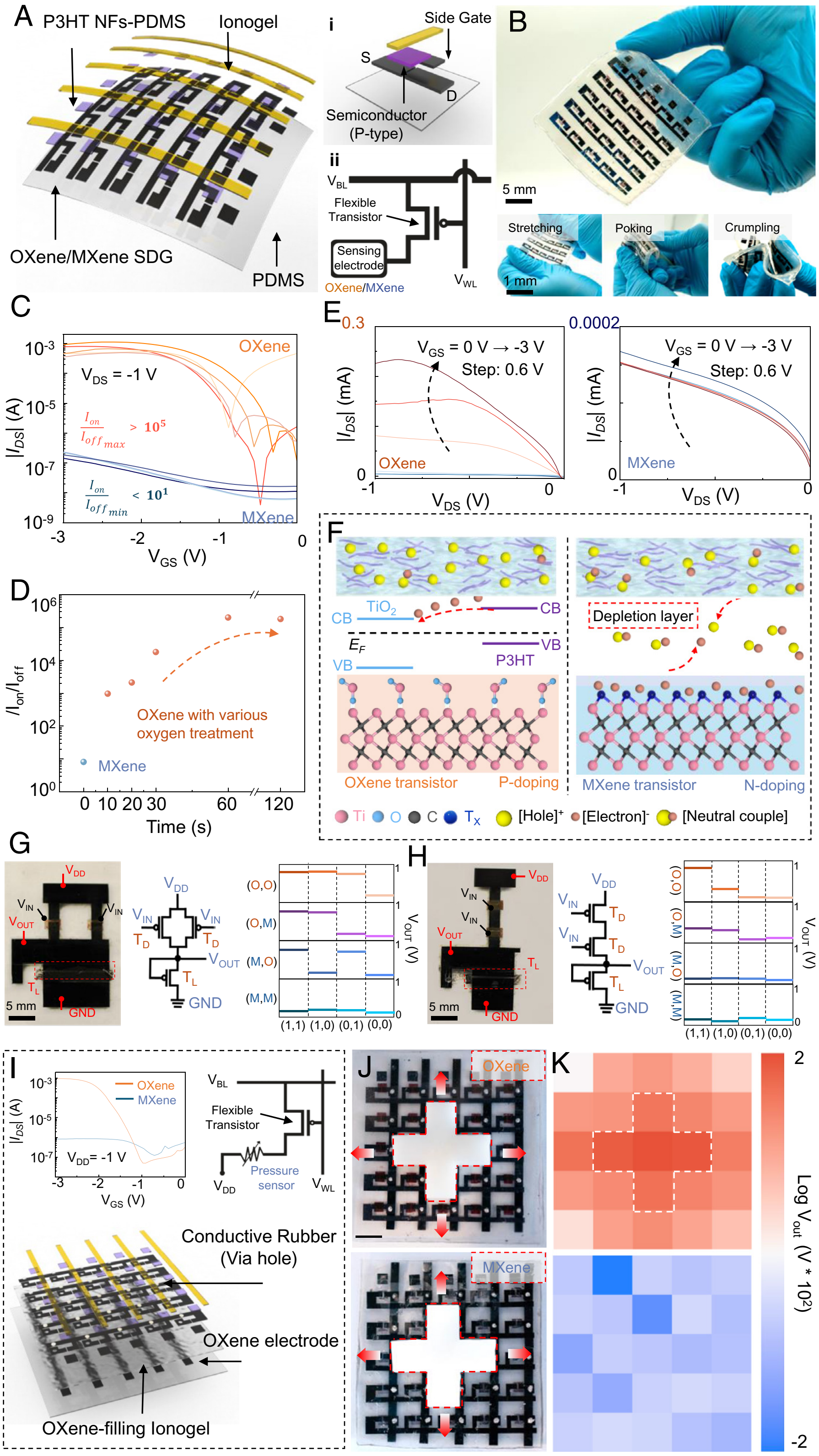

Fig. 4. Symmetry engineering in OXene enables reconfigurable "0" and "1" logic interfaces as SDG layers in flexible transistor arrays. (*A*) An exploded schematic view of the 5 × 5 transistor array with OXene/MXene SDG layer. SDG, SDG layer. The constituent components include flexible PDMS (PDMS, 1:10) substrates, OXene or MXene traces serve as transistor interconnects, with poly(3-hexylthiophene-2,5-diyl) nanofibrils-PDMS (labeled as P3HT NFs-PDMS) as the semiconductor, and ionogel as the flexible dielectric layer. i) Schematic exploded view of the architecture of a transistor node. ii) The circuit diagram for a single sensory transistor in the active matrix. V_{BL}, bit line voltage; V_{WL}, word line voltage. (*B*) Optical image of transistor array under various mechanical deformations. (*C*) Representative transfer characteristics of the OXene/MXene transistors with a p-type P3HT NFs-PDMS semiconductor layer. The gate current ranged around 10^{-10} to 10^{-11} A is omitted. Distinct OXene curves are attributed to different oxygen plasma treatment periods (30 cc min^{-1}, power 200 W 40 KHz, ranging from 10 s to 120 s). I_{DS}, drain-source current; V_{DS}, drain-source voltage; V_{GS}, gate-source voltage. (*D*) Switching current ratios (I_{on}/I_{off}) of OXene transistors under various oxygen treatment periods, in comparison to MXene transistors without oxygen treatment. (*E*) Comparison of output characteristics of OXene (oxygen plasma treatment: 60 s) and MXene transistors. (*F*) Schematic illustration of the principle of OXene (*Left*) and MXene (*Right*) SDG as a reconfigurable computational substrate. Profile architecture on the OXene transistor illustrates the electron transfer from CB of P3HT to CB of TiO_2, featuring further P-doping in P-type P3HT. Upon the MXene transistor, the negatively charged MXene surface anchors the holes in P3HT to form the depletion layer, corresponding to executing N-doping in P-type P3HT. CB, conduction band; VB, valence band; E_F, Fermi energy level. (*G* and *H*) Logic gates constructed from OXene and MXene as the SDG layer, P3HT NFs-PDMS as the semiconductor layer, and ionogels as the dielectric layer. Optical image (*Left*), circuit diagram (*Medium*), and output characteristics (*Right*) of the (*G*) NAND gate and (*H*) NOR gate under V_{DD} of 1 V. The input voltages (V_{IN}) of −3 or 0 V represent logic states 1 or 0, respectively. Selective oxidation of S-D region on two T_D is operated by a shadow mask. T_D, driver transistor; T_L, loading transistor. (*I*) Schematic exploded view of the active matrix for pressure sensing. Differing from *A*, the key components OXene-filled ionogel, OXene *Bottom* electrode, and conductive via holes implement the epitaxial Drain and pressure-sensitive signaling transmission. (*Inset*: *Left*) Transfer characteristics of one pressure-sensitive pixel in the active matrix with OXene or MXene SDG layer; (*Right*) The circuit diagram of one pressure-sensitive pixel. (*J*) Optical image of the pressure-sensitive active matrix featuring OXene (*Upper*) and MXene (*Down*) SDG layer in contact with the identical block. (Scale bar, 5 mm.) (*K*) Corresponding distributive voltage mapping result gathering from OXene (*Upper*) and MXene (*Down*) transistor array. The data are plotted as the means with n = 5 per unit corresponding to SD. Note: Scalebar optimizes data visualization through logarithmic axes while highlighting data differences between OXene and MXene active matrix.

real-time heartbeat interval monitoring and captures the dynamic amplitude of myocardial contractions (Fig. 5*F* and Movie S5).

The scalability of OXene promises spatiotemporal resolved mapping via active-matrix multiplexing. We devise a 16-channel synchronous pressure patch mounted on the myocardium (Fig. 5*G*), leveraging OXene's optimized interfacial impedance and piezoelectric effects for conductive plates and sensing pixels (*SI Appendix*, Fig. S26*A*). Signal processing was achieved by sequentially filtering out ambient and motion-related noise (*SI Appendix*, Fig. S26*B*), then interpolating to illustrate the myocardial contractile propagation within each time frame (Fig. 5*H*). The 3D stacked mapping (Fig. 5*I* and *SI Appendix*, Fig. S26 *C* and *D*) vividly contrasts pressure variations between sinus rhythm and MI states, assessing alterations in cardiac contraction amplitude and rhythm due to myocardial damage and fibrosis. This approach allows for the precise identification of regions with cyclic

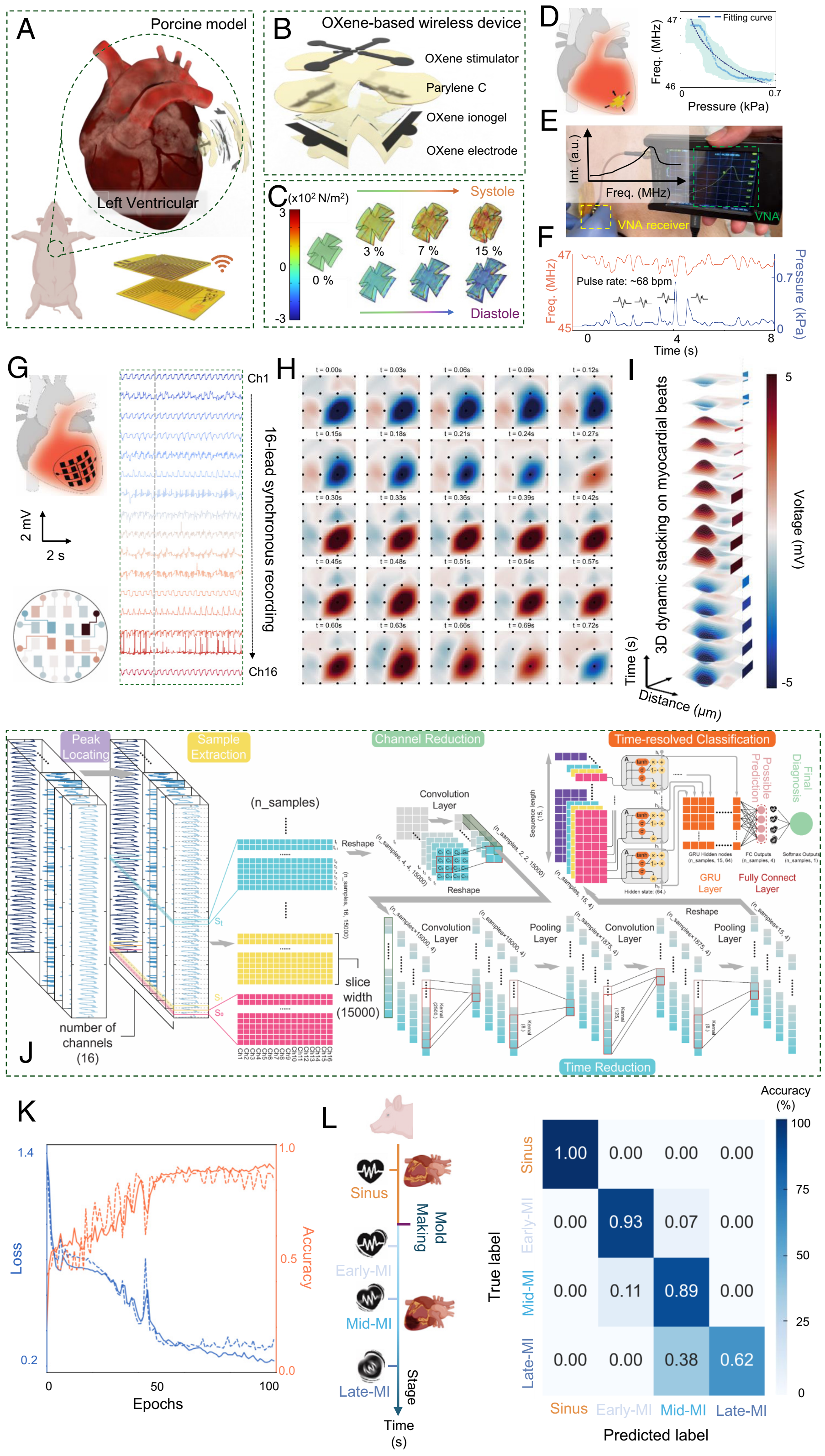

Fig. 5. Symmetry engineering in OXene realizes real-time, spatiotemporally resolved, wireless bioelectronic interfaces, featuring ML-powered physiological response prediction. (*A*) Schematic illustration of an OXene-based wireless device deployed onto a porcine heart near the Left ventricle. (*Inset*) Radiofrequency (RF) coil for electrotherapy and RF coil for strain sensing. Both RF coils are placed subcutaneously for optimized signal transmission. (*B*) Exploded schematic illustration of a wireless OXene patch integrated with a pressure sensor and an electrical stimulator. The upper electrical stimulator consists of four surrounding electrodes and a central reference, all based on OXene traces, encapsulated by parylene C via shadow masks. The pressure sensor is composed of two electrodes based on OXene traces, OXene-filled ionogels, and the parylene C encapsulation layer. (*C*) Simulated strain distribution using 3D finite element analysis to show the mechanical performance of the pressure module under myocardium systole and diastole. Convergence of meshes was tested to ensure computational accuracy. 5% initial deformation was set considering the device size and conformal adherence to the epicardial surface. (*D*) Measured calibration curve between signal frequency and pressure using an in vitro setup. The setup features a 25 mm × 10 mm × 3 mm (L × W × H) medium, undergoing the time-synchronized stretch curves of OXene-filled ionogels. (*E*) Optical image of OXene patch undergoing wireless and real-time detection in vivo to highlight contractility and heartbeat intervals upon MI-molding porcine hearts received by the VNA 1 wk after implantation. VNA: vector network analyzer. (*F*) Measured resonant frequency gathered from in vivo MI model monotonically converted to the pressure applied to the sensor under time-synchronized segments. The wireless OXene patch monitors the long-term process of cardiac tissue remodeling after an episode of MI. (*G*) Representative real-time synchronous recording of the OXene patch on a porcine heart in the sinus state. Voltage output was recorded by the 16 pressure-sensitive pixels on the OXene patch at a continuous frame of the data stream. The signals were processed through high-pass, low-pass, and bandstop filtering. (*H*) Interpolated spatial mapping of the detected pressure featuring sinus signals within a cardiac cycle (~0.72 s, Interval = 30 ms). (*I*) Corresponding 3D dynamic mappings of sinus state during myocardial contractile propagation superimposed by interpolation and normalization. Specifically, a red bar exhibits an average pressure higher than the baseline, while vice versa signifies a lower average pressure. The X-Y plane shows the spatial distribution of each sensing unit. The vertical direction depicts the time stream, at a time interval of 30 ms per frame. (*J*) Schematic architecture of the deep-learning classification algorithm. The process starts from *Left* to *Right*: peak locating algorithm that locates the temporal locations of heart pulsation peaks; sample extraction algorithm that slices down the signals into small windows; convolution layer that reduces the number of channels and shortens the sequential lengths; GRU layer to analyze the temporal trend of the data. The algorithm yields a score for all four labels (sinus, early-MI, mid-MI, late-MI) and draws a conclusion based on the label with the highest score. (*K*) Training curves of the deep-learning model. Solid lines show the training data while the dashed lines show the test data. Blue lines: Loss curves. Orange lines: accurate curves. (*L*, *Left*) Schematic illustration of four selected data segments, labeling as Sinus, Early-MI, Mid-MI, and Late-MI. Each segment is 10 s in length. *Right*: The confusion matrix for the model performance. *Y*-axis: true label (Sinus through Late-MI, from top to bottom), *X*-axis: predicted label (Sinus through Late-MI, from left to right).

contraction, especially from local myocardial ischemia post-MI (*SI Appendix*, Fig. S26 *E* and *F* and Movie S6).

The spatiotemporal mapping facilitates the classification and prediction of MI stages using a convolutional neural network-gated recurrent unit (CNN-GRU) architecture. This network, illustrated in Fig. 5*J*, begins with preprocessing that includes peak location and sample extraction to register data slices for subsequent analysis (*SI Appendix*, Fig. S27). Thereafter, dual convolution networks serve to encode both spatial and temporal dimensions. Eventually, the GRU network is used to predict the MI status based on the processed data. The CNN-GRU model demonstrates promising convergence, achieving a training accuracy of 89.4% with a loss of 0.229, and testing accuracy of 84.5% with a loss of 0.351 (Fig. 5*K*). The algorithm distinctly differentiates between sinus rhythm and various stages of MI—early, middle, and late (Fig. 5*L*). The spatiotemporally resolved OXene-integrated signal is capable of predicting adverse clinical events using the ML pipeline, while enabling detailed patient screening and progression monitoring.

OXene and its constituent devices feature superior biocompatibility over other common bioelectrical materials (e.g., Au and PEDOT:PSS). This is supported by cytotoxicity assays including the cell Counting Kit-8 (CCK8) (*SI Appendix*, Fig. S28*B*) and Live/Dead assays (*SI Appendix*, Fig. S28*C*) with neonatal rat cardiomyocytes (NRCMs), showing minimal impact on cardiomyocyte viability over 48 h of co-culturing. To assess the level of inflammation in the heart following open-chest surgery and OXene implantation, we used immunohistochemistry to assess short-term (CD68, CD11b) and long-term (CD3) inflammation markers (*SI Appendix*, Fig. S29). Quantification of OXene implants shows lower levels of inflammation than others after implantation, indicating that the OXene and associated implantation surgery do not provoke an inflammatory response. Histological examination of tissue adjacent to the OXene device up to 2 wk post-implantation employed Masson's trichrome staining to identify fibrotic areas (*SI Appendix*, Fig. S30). The quantification of fibrotic tissue thickness presents OXene with significantly lower fibrosis than Au and PEDOT:PSS (*SI Appendix*, Fig. S30*B*). The results indicate normal tissue structure, with marginal fibrosis confined to the tissue's outer layers at the device contact point. Overall, results show that OXene induces minimal cytotoxicity, inflammation, and fibrosis in vivo.

Conclusion

We harnessed symmetry engineering to augment 2D bioelectronic interfaces. By coupling orbital and inverse symmetric breaking, OXene achieves decreased electronic-tissue impedance and Schottky-induced piezoelectric effects. These features enable OXene's applicability to different domains, including bioelectrode arrays, gait analysis, and wireless cardiac patches, allowing for multiplexed, high-fidelity, and spatiotemporally resolved physiological recordings in both rodent and porcine models. Integration with ML pipelines demonstrates accurate physiological state classification and prediction. Simultaneously the interface-polarized OXene can be integrated with MXene to achieve distinctive reconfiguration computational substrates in active matrix, promising a flattened programmable dimension for dense, swift, and energy-efficient bioelectronic frameworks. On a broader way, the symmetry modulation allows for numerous augmented 2D bioelectronics interfaces. This design principle may offer a groundbreaking attainment upon existing 2D bioelectronics, especially in clinical practice.

Materials and Methods

A detailed account of Materials and Methods used in this study can be found in *SI Appendix*. This includes the synthesis and characterization processes for OXene-based bioelectronics, such as the fabrication and mechanical testing of OXene-filled ionogels. supplementary material also covers the preparation of P3HT-NFs/PDMS composites, ionogel dielectrics, and the development of OXene-mediated transistors, as well as NAND and NOR gate arrays. Additionally, electrochemical characterization techniques, preparation protocols for EXAFS, and procedures for cytotoxicity and biocompatibility assessments are described. Various material characterization methods, including AFM, XRD, Raman spectroscopy, and XPS, along with computational approaches like DFT calculations, are thoroughly detailed. The section also includes methods for device characterization in animal experiments, statistical analysis, and simulations for wireless power transfer and electromagnetic resonance sensing. Readers are encouraged to refer to *SI Appendix* for a comprehensive description of these procedures.

Data, Materials, and Software Availability. All data needed to evaluate the conclusions in the manuscript are present in the manuscript and/or *SI Appendix*.

ACKNOWLEDGMENTS. This work was supported by the start-up funds from University of North Carolina at Chapel Hill and the fund from NSF (Award # ECCS-2139659). Research reported in this publication was also supported by the National Institute of Biomedical Imaging and Bioengineering at the NIH under Award No. 1R01EB034332-01.

Author affiliations: [a]Department of Applied Physical Sciences, University of North Carolina, Chapel Hill, NC 27599; [b]Joint Department of Biomedical Engineering, University of North Carolina at Chapel Hill, Chapel Hill, NC 27599; [c]Joint Department of Biomedical Engineering, North Carolina State University, Raleigh, NC 27695; [d]Department of Computer Science, University of North Carolina at Chapel Hill, Chapel Hill, NC 27599; [e]Department of Physics, Nanjing University, Nanjing, Jiangsu 210000, China; [f]Department of Biomedical Engineering, Columbia University, New York, NY 10027; [g]Department of Computer Science and Engineering, Michigan State University, East Lansing, MI 48824; [h]Department of Molecular Biomedical Sciences, North Carolina State University, Raleigh, NC27607; [i]Wide Bandgap Semiconductor Technology Disciplines State Key Laboratory, Department of Advanced Interdisciplinary Research, Xidian University, Xi'an 710071, China; [j]Department of Psychiatry, University of North Carolina at Chapel Hill, Chapel Hill, NC 27599; [k]Department of Statistics and Operations Research, University of North Carolina at Chapel Hill, Chapel Hill, NC 27599; and [l]Neuroscience Center, Department of Medicine, University of North Carolina at Chapel Hill, Chapel Hill, NC 27599

Author contributions: Y. Wu, Z.G., and W.B. designed research; Y. Wu, Y. Liu, Y. Li, D.Z., A.Z., and G.Y. performed research; Y. Wu, K.H., Yong Wang, G.W., K.C., and W.B. contributed new reagents/analytic tools; Y. Wu, Y. Liu, Z.W., S.X., Yunlang Wang, D.Z., A.Z., Z.Z., Yong Wang, and W.B. analyzed data; and Y. Wu, Y. Li, Z.W., S.X., and W.B. wrote the paper.

The authors declare no competing interest.

1. C. Choi, Y. Lee, K. W. Cho, J. H. Koo, D. H. Kim, Wearable and implantable soft bioelectronics using two-dimensional materials. *Acc. Chem. Res.* **52**, 73–81 (2019).
2. D. Kireev, A. Offenhäusser, Graphene & two-dimensional devices for bioelectronics and neuroprosthetics. *2D Mater.* **5**, 042004 (2018).
3. Y. Liu, A. Offenhäusser, D. Mayer, Rectified tunneling current response of bio-functionalized metal-bridge-metal junctions. *Biosens. Bioelectron.* **25**, 1173–1178 (2010).
4. J. Li *et al.*, A tissue-like neurotransmitter sensor for the brain and gut. *Nature* **606**, 94–101 (2022).
5. X. Zhao *et al.*, Permanent fluidic magnets for liquid bioelectronics. *Nat. Mater.* **23**, 703–710 (2024).
6. W. Zhou *et al.*, Soft and stretchable organic bioelectronics for continuous intraoperative neurophysiological monitoring during microsurgery. *Nat. Biomed. Eng.* **7**, 1270–1281 (2023).
7. J. Yin *et al.*, Motion artefact management for soft bioelectronics. *Nat. Rev. Bioeng.* **2**, 541–558 (2024).
8. E. Song, J. Li, S. M. Won, W. Bai, J. A. Rogers, Materials for flexible bioelectronic systems as chronic neural interfaces. *Nat. Mater.* **19**, 590–603 (2020).
9. S. Park *et al.*, Self-powered ultra-flexible electronics via nano-grating-patterned organic photovoltaics. *Nature* **561**, 516–521 (2018).
10. R. Liu, Z. L. Wang, K. Fukuda, T. Someya, Flexible self-charging power sources. *Nat. Rev. Mater.* **7**, 870–886 (2022).
11. S. W. Cheong, SOS: Symmetry-operational similarity. *npj Quant. Mater.* **4**, 53 (2019).
12. S. Harimurti *et al.*, Janus electrode with stable asymmetric wettability for robust biosignal monitoring on sweaty skin. *Mater. Today* **74**, 94–108 (2024).
13. P. Zubko, G. Catalan, A. K. Tagantsev, Flexoelectric effect in solids. *Annu. Rev. Mater. Res.* **43**, 387–421 (2013).
14. Y. Ding *et al.*, Cellulose tailored anatase TiO_2 nanospindles in three-dimensional graphene composites for high-performance supercapacitors. *ACS Appl. Mater. Interfaces* **8**, 12165–12175 (2016).
15. S. Moser *et al.*, Tunable polaronic conduction in anatase TiO_2. *Phys. Rev. Lett.* **110**, 196403 (2013).
16. A. Grimaud *et al.*, Double perovskites as a family of highly active catalysts for oxygen evolution in alkaline solution. *Nat. Commun.* **4**, 2439 (2013).
17. S. Lany, Semiconducting transition metal oxides. *J. Phys. Condens. Matter.* **27**, 283203 (2015).
18. X. Wang *et al.*, Pseudocapacitance of MXene nanosheets for high-power sodium-ion hybrid capacitors. *Nat. Commun.* **6**, 6544 (2015).
19. M. M. Yang *et al.*, Piezoelectric and pyroelectric effects induced by interface polar symmetry. *Nature* **584**, 377–381 (2020).
20. R. Guo *et al.*, Interface-engineered electron and hole tunneling. *Sci. Adv.* **7**, eabf1033 (2021).
21. Z. Zhu, J. Qi, X. Zheng, X. Lin, W. Li, Polar discontinuities and interfacial electronic properties of Bi_2O_2Se on $SrTiO_3$. *Phys. Rev. B* **108**, 245304 (2023).
22. O. Aktas *et al.*, Piezoelectricity in nominally centrosymmetric phases. *Phys. Rev. Res.* **3**, 043221 (2021).
23. J. Yu, C. X. Liu, Piezoelectricity and topological quantum phase transitions in two-dimensional spin-orbit coupled crystals with time-reversal symmetry. *Nat. Commun.* **11**, 2290 (2020).
24. G. C. Li *et al.*, Light-induced symmetry breaking for enhancing second-harmonic generation from an ultrathin plasmonic nanocavity. *Nat. Commun.* **12**, 4326 (2021).
25. H. Ryu *et al.*, Materials and design approaches for a fully bioresorbable, electrically conductive and mechanically compliant cardiac patch technology. *Adv. Sci.* **10**, 2303429 (2023).
26. M. Wang *et al.*, Tough and stretchable ionogels by in situ phase separation. *Nat. Mater.* **21**, 359–365 (2022).

27. Y. Shu *et al.*, Efficient ohmic contact in monolayer CrX_2N_4 (X = C, Si) based field-effect transistors. *Adv. Electron. Mater.* **9**, 2201056 (2023).
28. S. M. Sze, Y. Li, K. K. Ng, *Physics of Semiconductor Devices* (John Wiley & Sons, 2021).
29. J. Shi, P. Zhao, X. Wang, Piezoelectric-polarization-enhanced photovoltaic performance in depleted-heterojunction quantum-dot solar cells. *Adv. Mater.* **25**, 916–921 (2013).
30. Y. He, Y. Cheng, C. Yang, C. F. Guo, Creep-free polyelectrolyte elastomer for drift-free iontronic sensing. *Nat. Mater.* **23**, 1107–1114 (2024).
31. C. Pan *et al.*, Reconfigurable logic and neuromorphic circuits based on electrically tunable two-dimensional homojunctions. *Nat. Electron.* **3**, 383–390 (2020).
32. B. Lyu *et al.*, Large-area mxene electrode array for flexible electronics. *ACS Nano* **13**, 11392–11400 (2019).
33. C. Erdmann *et al.*, A heterogeneous 3D-IC consisting of two 28 nm FPGA die and 32 reconfigurable high-performance data converters. *IEEE J. Solid-State Circ.* **50**, 258–269 (2015).
34. Y. S. Choi *et al.*, A transient, closed-loop network of wireless, body-integrated devices for autonomous electrotherapy. *Science* **376**, 1006–1012 (2022).
35. S. M. Won, L. Cai, P. Gutruf, J. A. Rogers, Wireless and battery-free technologies for neuroengineering. *Nat. Biomed. Eng.* **7**, 405–423 (2023).
36. E. C. H. van Doorn *et al.*, Preclinical models of cardiac disease: A comprehensive overview for clinical scientists. *Cardiovasc. Eng. Technol.* **15**, 232–249 (2024).
37. J. W. Song *et al.*, Bioresorbable, wireless, and battery-free system for electrotherapy and impedance sensing at wound sites. *Sci. Adv.* **9**, eade4687 (2023).